ARL-TN-1282 ● Oct 2025

Demonstration of the Stress Corrosion Resistance of Precipitation-Hardenable 5XXX Series Alloy AA5180

by Taylor W. Cain

NOTICES

Disclaimers

The findings in this report are not to be construed as an official Department of the Army position unless so designated by other authorized documents.

Citation of manufacturer's or trade names does not constitute an official endorsement or approval of the use thereof.

Destroy this report when it is no longer needed. Do not return it to the originator.

ARL-TN-1282 ● OCT 2025

Demonstration of the Stress Corrosion Resistance of Precipitation-Hardenable 5XXX Series Alloy AA5180

Taylor W. Cain
DEVCOM Army Research Laboratory

REPORT DOCUMENTATION PAGE

1. REPORT DATE	2. REPORT TYPE	3. DATES COVERED	
		START DATE	END DATE
October 2025	Technical Note	1 March 2023	30 September 2024

4. TITLE AND SUBTITLE
Demonstration of the Stress Corrosion Resistance of Precipitation-Hardenable 5XXX Series Alloy AA5180

5a. CONTRACT NUMBER	5b. GRANT NUMBER	5c. PROGRAM ELEMENT NUMBER
5d. PROJECT NUMBER	**5e. TASK NUMBER**	**5f. WORK UNIT NUMBER**

6. AUTHOR(S)
Taylor W. Cain

7. PERFORMING ORGANIZATION NAME(S) AND ADDRESS(ES)
DEVCOM Army Research Laboratory
ATTN: FCDD-RLA-MF
Aberdeen Proving Ground, MD 21005

8. PERFORMING ORGANIZATION REPORT NUMBER
ARL-TN-1282

9. SPONSORING/MONITORING AGENCY NAME(S) AND ADDRESS(ES)	10. SPONSOR/MONITOR'S ACRONYM(S)	11. SPONSOR/MONITOR'S REPORT NUMBER(S)

12. DISTRIBUTION/AVAILABILITY STATEMENT
DISTRIBUTION STATEMENT A. Approved for public release: distribution unlimited.

13. SUPPLEMENTARY NOTES
ORCID: Taylor W. Cain, 0000-0002-6621-914X

14. ABSTRACT
C-ring stress corrosion testing was performed on precipitation-hardenable Al-Mg-Zn-Cu alloy 5180 with a low (≈0.1 wt%) and high (≈0.225 wt%) Cu concentration in accordance with MIL-DTL-46027M. Samples in the as-received F-temper and solution-treated, water-quenched, and peak-aged T6-temper were found to survive the 96-h minimum requirement specified in MIL-DTL-46027M due to their exceptional ductility (>17% elongation to failure). Samples in the T6 condition failed after 15 days while samples in the F-temper did not fail after 28 days of testing. The discrepancy between tempers was linked to increased susceptibility of the T6-temper to intergranular corrosion attack, whereas no deviation between Cu content was observed.

15. SUBJECT TERMS
crossover alloy, 5XXX series alloy, precipitation hardenable, stress corrosion, Sciences of Extreme Materials

16. SECURITY CLASSIFICATION OF:			17. LIMITATION OF ABSTRACT	18. NUMBER OF PAGES
a. REPORT	b. ABSTRACT	C. THIS PAGE		
UNCLASSIFIED	UNCLASSIFIED	UNCLASSIFIED	UU	31

19a. NAME OF RESPONSIBLE PERSON	19b. PHONE NUMBER *(Include area code)*
Taylor W. Cain	(520) 691-5035

STANDARD FORM 298 (REV. 5/2020)
Prescribed by ANSI Std. Z39.18

Contents

List of Figures

List of Tables

1. Introduction

The development of novel 5XXX series aluminum-magnesium (Al-Mg)-based alloys is of great interest to the defense community for both land and sea applications due to their light weight, medium strength, good weldability, and good corrosion resistance.[1] Recent publications in open literature have shown rapid interest and development of high-strength, precipitation-hardenable 5XXX series alloys that are Al-Mg-Zn-Cu based.[2–35] This new subclass of alloys, dubbed "crossover" alloys, contains elevated levels of Zn in the alloys compared with traditional 5XXX series alloys, which nominally shift the equilibrium phase field from α + ß to an α + τ phase field. This change in equilibrium phase field is important for multiple reasons. First, precipitation hardening adds more strength than conventional 5XXX alloys, which are only strengthened by solid solution strengthening of Mg additions and cold work via rolling and/or stretching. Second, precipitation of the ß-phase along grain boundaries at temperatures below 100 °C has long been known to be a problem with 5XXX series alloys due to increased susceptibility of intergranular corrosion (IGC), which leads to decreased strength and elevated risk of catastrophic cracking due to environmentally assisted cracking (EAC).[36–39] This phenomenon, known as sensitization, has not been as prominent in crossover alloys with some alloy compositions showing immunity.[10,19,24,35] Third, crossover alloys have shown the ability to not suffer from hot cracking and possess high-welded strengths[20,27,28] in addition to resistance to stress corrosion cracking (SCC).[7,34] However, further research is needed to fully understand EAC behavior of crossover alloys and how they compare with conventional 5XXX series alloys.

The goal of this study was to determine the susceptibility of crossover alloy 5180 to SCC as a function of Cu concentration because the susceptibility of Al alloys to SCC is sensitive to Cu content. Two different compositions of 5180 were evaluated on plate in a hot rolled condition (F-temper) and in a solution-treated, water-quenched, and peak-aged condition (T6-temper). Stress corrosion testing was performed using C-ring test specimens subjected to an alternate immersion test procedure in a neutral NaCl environment according to the requirements of MIL-DTL-46027M[40] In addition, samples were characterized for their mechanical properties, microstructure, and general corrosion resistance.

2. Methods and Procedures

In this investigation, AA5180 was evaluated with two different levels of Cu whose actual composition, as measured by inductively coupled plasma-optical emission spectroscopy (ICP-OES), can be found in Table 1. Here, the final Cu compositions were 0.104 wt% for alloy 2A2 and 0.226 wt% for alloy 2B. The alloys were first direct chill cast, sectioned into rolling blocks, scalped, homogenized, hot rolled from 3.75 inches to a final thickness of 1.5 inches, and forced air cooled to produce the F-temper plate. The final plates for this study are shown in Figure 1 with the rolling direction (RD) and transverse direction (TD) labeled on the image.

Table 1. Composition of each alloy as measured by ICP-OES in wt%.

Alloy	Al	Mg	Zn	Cu	Mn	Zr	Ti	Fe	Cr	Ni	Si	Sc
2A2	Bal	3.850	2.309	0.104	0.191	0.138	0.088	0.039	0.002	0.005	0.063	0.037
2B	Bal	3.953	2.286	0.226	0.191	0.148	0.096	0.041	0.002	0.006	0.078	0.037

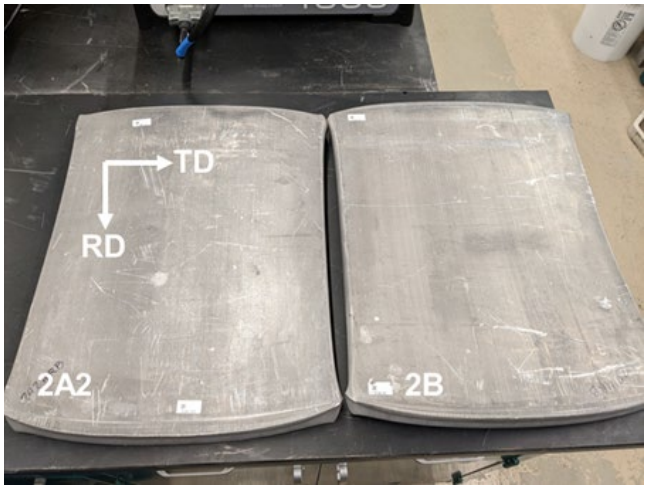

Figure 1. The as-received plates with the RD and TD labeled for alloy 2A2 and 2B.

The quasi-static tensile mechanical properties of each alloy plate were determined using 0.25-inch-thick, ASTM B557[41] subsize dog bone tensile specimens cut in the TD of the plates (Figure 2). Samples were tested in both the F-temper and the peak-aged T6-temper. In addition, Rockwell B hardness (HRB) was performed on the rolled surface and at one half the thickness of the plate to evaluate through-thickness mechanical properties. The T6-temper was produced by solution treating samples (dog bone and C-ring) at 485 °C for 1 h in a muffle furnace, water quenching, and dual step ageing at 90 °C for 24 h followed by 140 °C for 48 h in a convection oven. After completion of the 48-h time step, samples were removed from the oven and allowed to air cool.

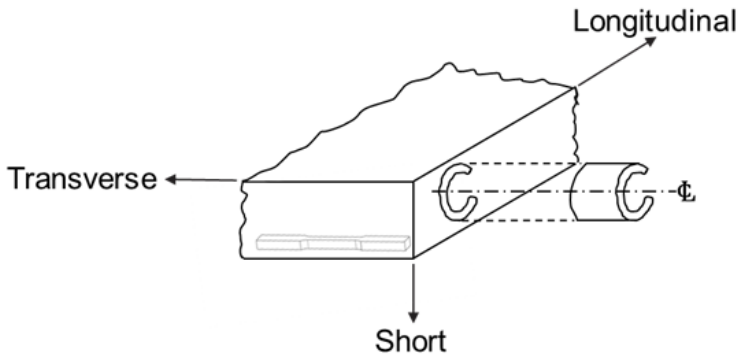

Figure 2. The orientation of transverse tensile specimens and C-ring specimens prepared from the as-received plate. The symbol ℄ indicates the centerline of short direction in the plate.

The microstructure of each alloy in the F-temper and T6-temper were investigated using multiple microscopy methods. Optical microscopy was performed on a KEYANCE VK-X1100 optical profilometer, whereas scanning electron microscopy (SEM) was performed at an accelerating voltage of 20 kV operated in backscattered electron (BSE) mode on a Hitachi SU3500. Energy-dispersive X-ray spectroscopy (EDS) was performed using the Bruker QUANTAX EDS system attached to the SU3500. All samples were hot mounted using Stuers Polyfast and ground to a 1200-grit CAMI (Coated Abrasives Manufacturing Institute) finish using silicon carbide grinding papers. Samples were then polished successively using water-based, 1- and 0.25-μm diamond slurries while rinsing with deionized (DI) water after each polishing step. Final polishing was completed using 0.05-μm Beuhler MasterPrep polishing suspension, rinsed with DI water, and gently swabbed with a DI water-saturated (sat) cotton swab to remove residual polishing slurry from the alloy surface. Polished surfaces were rinsed with ethanol and dried under a heated fan. Samples for optical microscopy were etched using Weck's reagent composed of 4 g $KMnO_4$ and 1 g NaOH/100-mL DI water. Samples were immersed for 90 s, rinsed with DI water, and dried with compressed nitrogen gas.

Stress corrosion testing was evaluated according to MIL-DTL-46027M,[40] which specifies the use of C-ring corrosion testing via ASTM G38[42] and G47.[43] C-rings were prepared following ASTM G38[42] with samples having an outside diameter of 1 inch and thickness of 0.075 inch oriented in the short-transverse (ST) direction as shown in Figure 2.[*] Samples were preloaded to either 30 ksi per MIL-DTL-46027M[40] or 35 ksi in some cases per MIL-DTL-32505B[44] (Table 2) by tightening a nut and bolt assembly to a specified strain as determined from the elastic portion of stress–strain curves generated from tensile testing in the ST direction. The nut

[*]The rolling direction of the plate is the same as the longitudinal (L) direction, the transverse direction is the transverse (T) direction, and the normal direction (ND) is the short (S) direction.

and bolt assembly was isolated from galvanic coupling by coating the sample surface with beeswax, leaving only the stressed area of the C-ring exposed to solution. The C-ring specimens were then placed vertically in an alternate immersion corrosion chamber as shown in Figure 3 and exposed to a repeating cycle of 10 min full immersion followed by 50 min of drying in pH = 7, naturally aerated, 3.5 wt% NaCl solution. The wet–dry cycle was carried out using submersible pumps, and the solution level was replenished with 18.2 MΩ DI water as needed to maintain constant NaCl concentration. In addition, the air temperature in the immersion chamber was maintained at 27 ± 1 °C and a relative humidity of 45% ± 10% per ASTM G44[45] for the duration of the test. Nine samples in each condition listed in Table 2 were tested. If a minimum of five of nine samples survived more than 96 h without cracking, then the alloy plate is deemed to pass minimum qualification standards for MIL-DTL-46027M[40] and MIL-DTL-32505B.[44]

Table 2. Applied load to each alloy and temper.

Alloy	Applied load
Alloy 2A2-F	30 ksi
Alloy 2A2-F	35 ksi
Alloy 2B-F	30 ksi
Alloy 2A2-T6	30 ksi
Alloy 2B-T6	30 ksi

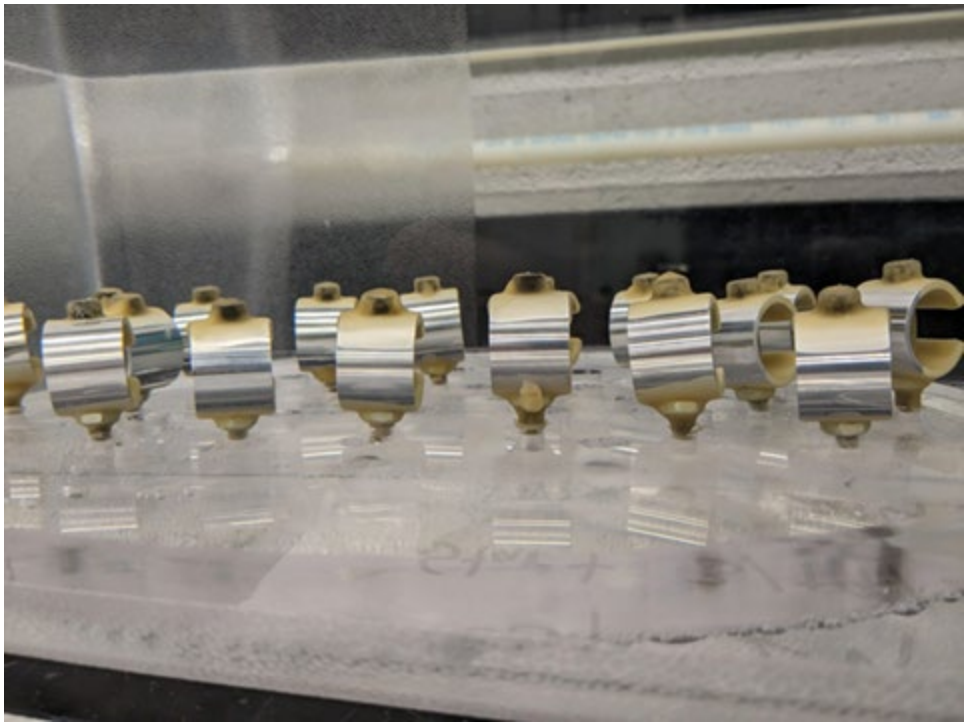

Figure 3. Placement of C-ring specimens in the test chamber.

The corrosion behavior of each alloy and temper was evaluated on the long-transverse (LT), long-short (LS), and ST planar surfaces in naturally aerated quiescent 3.5 wt% NaCl (pH = 6). Samples were allowed to rest at their open circuit potential (OCP) for 4 h and then polarized at a scan rate of 10 mV/min from −0.3 V versus OCP to +0.7 V versus OCP or to a current density of 10 mA/cm^2, whichever came first. An electrochemical flat cell with working electrode, platinum mesh counter electrode, and sat Ag/AgCl reference electrode with a working electrode area of 1 cm^2 was used for all electrochemical tests. A minimum of three replicates of each measurement was made to ensure repeatability.

3. Results and Discussion

3.1 Microstructure

The microstructure of each alloy was investigated using optical microscopy and SEM as shown in Figures 4–7. Images were taken on the planar face of the three principal directions to investigate texture and grain-size differences, which are well known to influence SCC. The optical image of alloy 2A2-F in Figure 4a revealed large, mostly equiaxed grains on the LT surface on the order of 100 μm in diameter with the grains becoming slightly elongated in the L direction. The grains showed a remnant dendritic morphology from the cast dendritic structure that was not broken up during homogenization and hot rolling of the plate. Meanwhile, the LS surface revealed grains that were elongated in the L direction while grains on the ST surface were mostly equiaxed and possessed the smallest grain diameters of the three surfaces. Backscattered SEM images of alloy 2A2-F revealed the presence of both bright and dark contrast areas along the grain boundaries as shown in Figure 4b. The dark phases were confirmed to not be pores via secondary electron imaging, indicating the presence of a light secondary phase. Compared with the alloy 2A2-F, the grain structure of alloy 2A2-T6 captured with optical microscopy did not show the remnant dendritic grain morphology in alloy 2A2-F, indicating further homogenization (Figure 5a). The grains did show a similar trend with slightly elongated grains in the L direction on the LT and LS surfaces with some grains becoming slightly elongated in the TD of the ST surface. The BSE images of alloy 2A2-T6 (Figure 5b) show a reduction in the total number of bright contrast phases along grain boundaries while the presence of the dark contrast phase remained after solution treatment. The observations made for alloy 2B are the same as those for alloy 2A2, as shown in Figures 6 and 7. Thus, further examination of the bright and dark contrast phases will only be presented for alloy 2B.

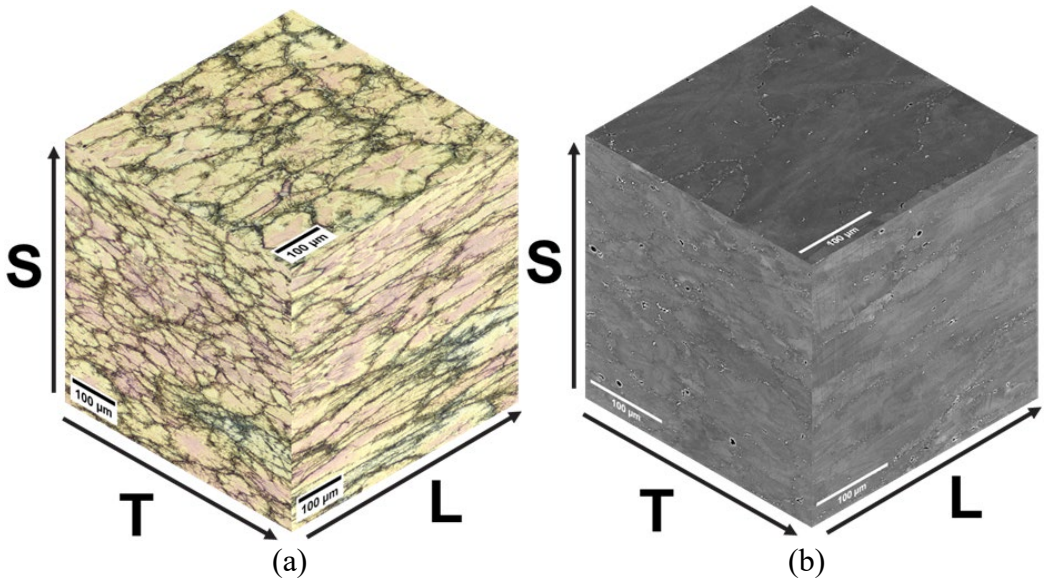

(a) (b)

Figure 4. Characteristic microscopy images of alloy 2A2-F using (a) optical microscopy and (b) BSE imaging. Scale bars are 100 µm.

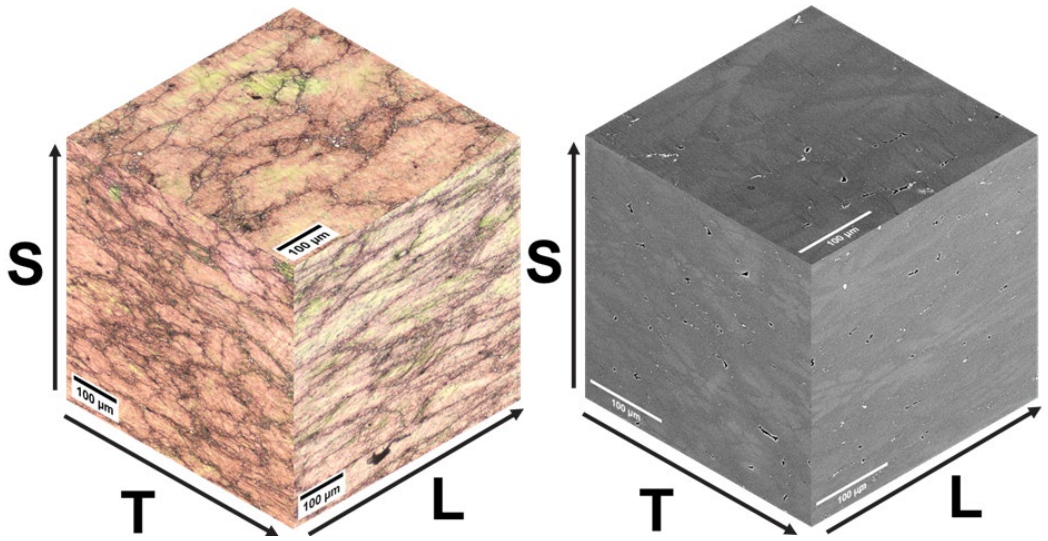

(a) (b)

Figure 5. Characteristic microscopy images of alloy 2A2-T6 using (a) optical microscopy and (b) BSE imaging. Scale bars are 100 µm.

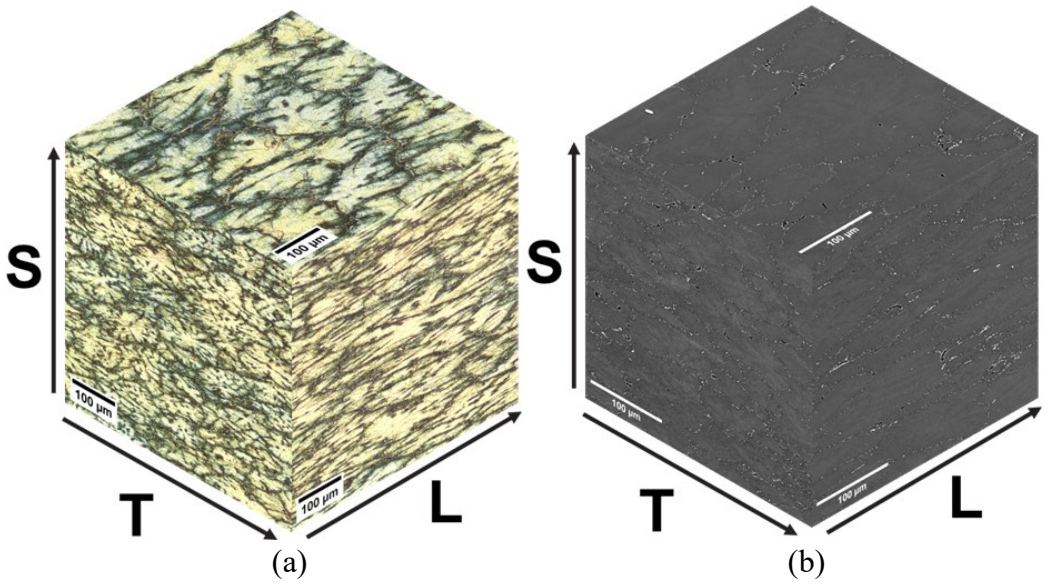

Figure 6. Characteristic microscopy images of alloy 2B-F using (a) optical microscopy and (b) BSE imaging. Scale bars are 100 µm.

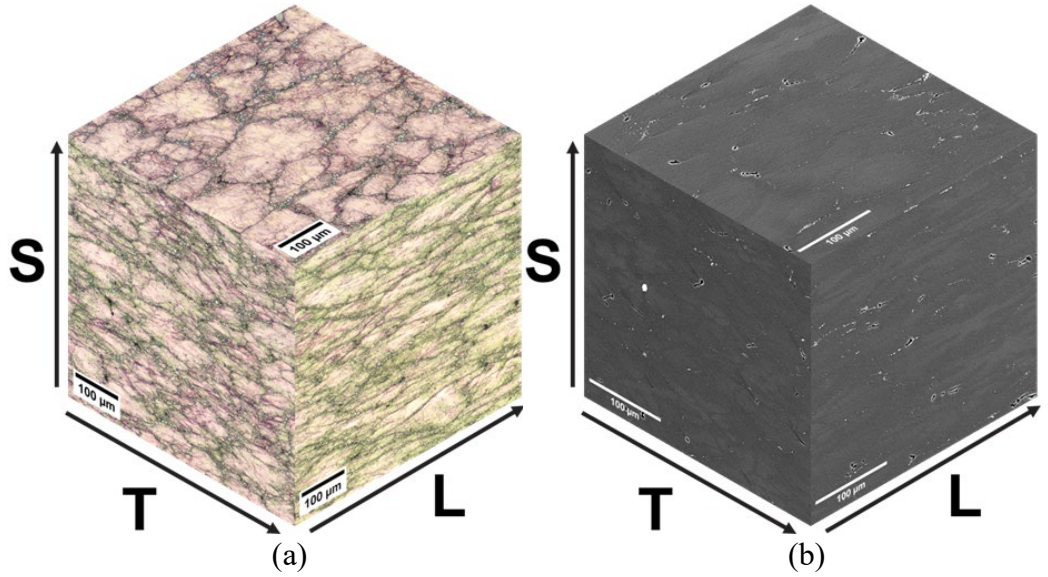

Figure 7. Characteristic microscopy images of alloy 2B-T6 using (a) optical microscopy and (b) BSE imaging. Scale bars are 100 µm.

Higher magnification BSE images were captured on alloy 2B-F accompanied by EDS mapping as shown in Figure 8. Three different phase morphologies were observed in the BSE image in the top left image: a very large bright contrast particle that was rich in Mn, Sc, Si, Ti, and Zr, very small bright contrast phases that were too small to be captured within the spatial resolution of EDS mapping at this magnification, and dark phases that were rich in Mg and Si. Point analysis of these dark phases provided a stoichiometry similar to that of Mg_2Si. The small bright phases were investigated at even higher magnification as shown in Figure 9 with

corresponding EDS elemental maps. These phases were rich in Mg and Zn, which indicates that they are likely to be either equilibrium τ-phase or a metastable variant. Figure 9 also shows the presence of an Mn-rich phase in the top left of the image, indicating formation of Al–Mn particles. These Al–Mn particles were observed throughout each sample along grain boundaries with a typical diameter between 1 and 10 µm. Investigation of higher magnification images of alloy in the T6 condition in Figure 10 did not show the presence of the (Mg, Zn)-rich phase along the grain boundaries, which indicated successful solution treatment of the T6 alloys. The only phases that were observed along grain boundaries were Mg_2Si and Al–Mn, which also showed incorporation of Fe (shown in Figure 10), which is typical of $Al_6(Mn,Fe)$. Further characterization of the nanostructure of each alloy by transmission electron microscopy was not completed as part of this study.

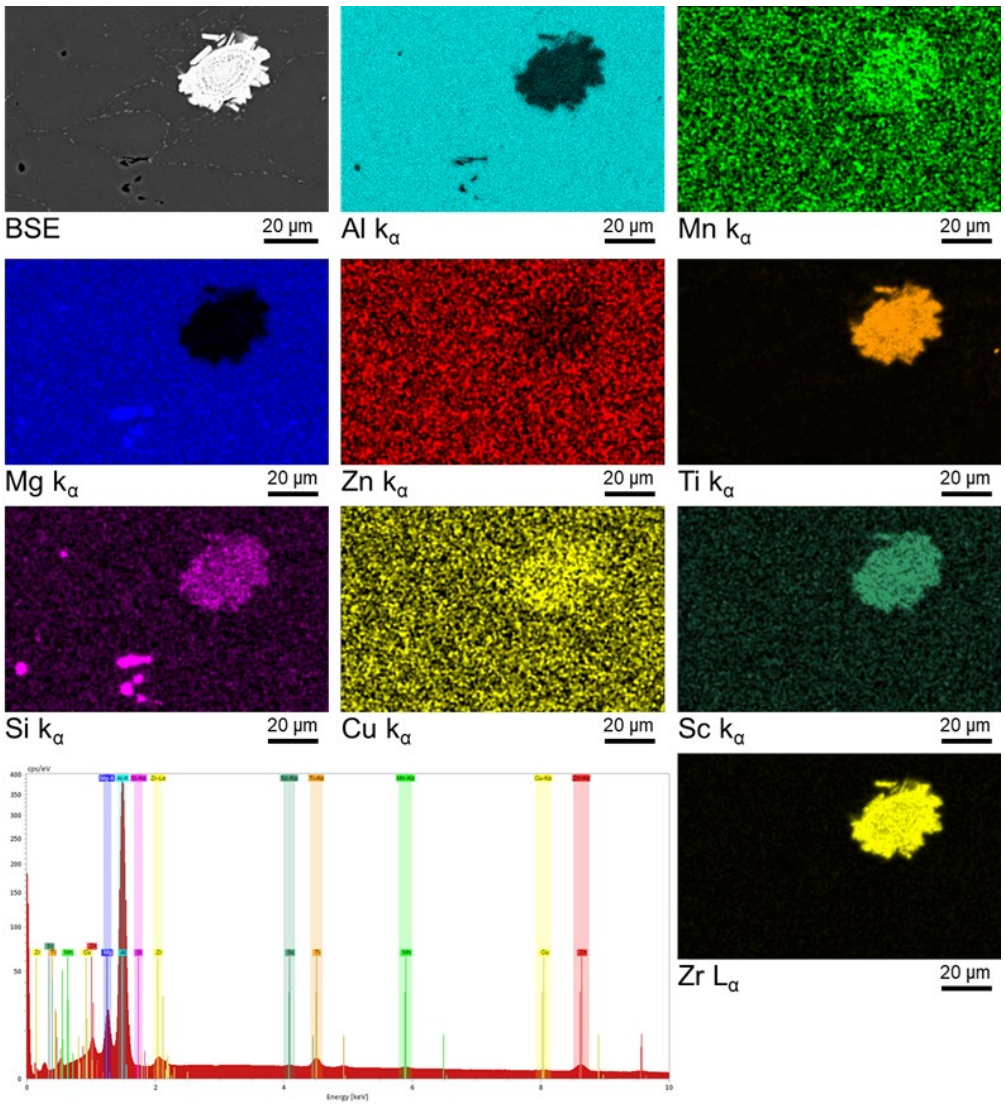

Figure 8. EDS mapping of large bright and dark contrast particles found on alloy 2B-F. k_α energies were used to construct maps of all elements except for Zr, which used the L_α energies.

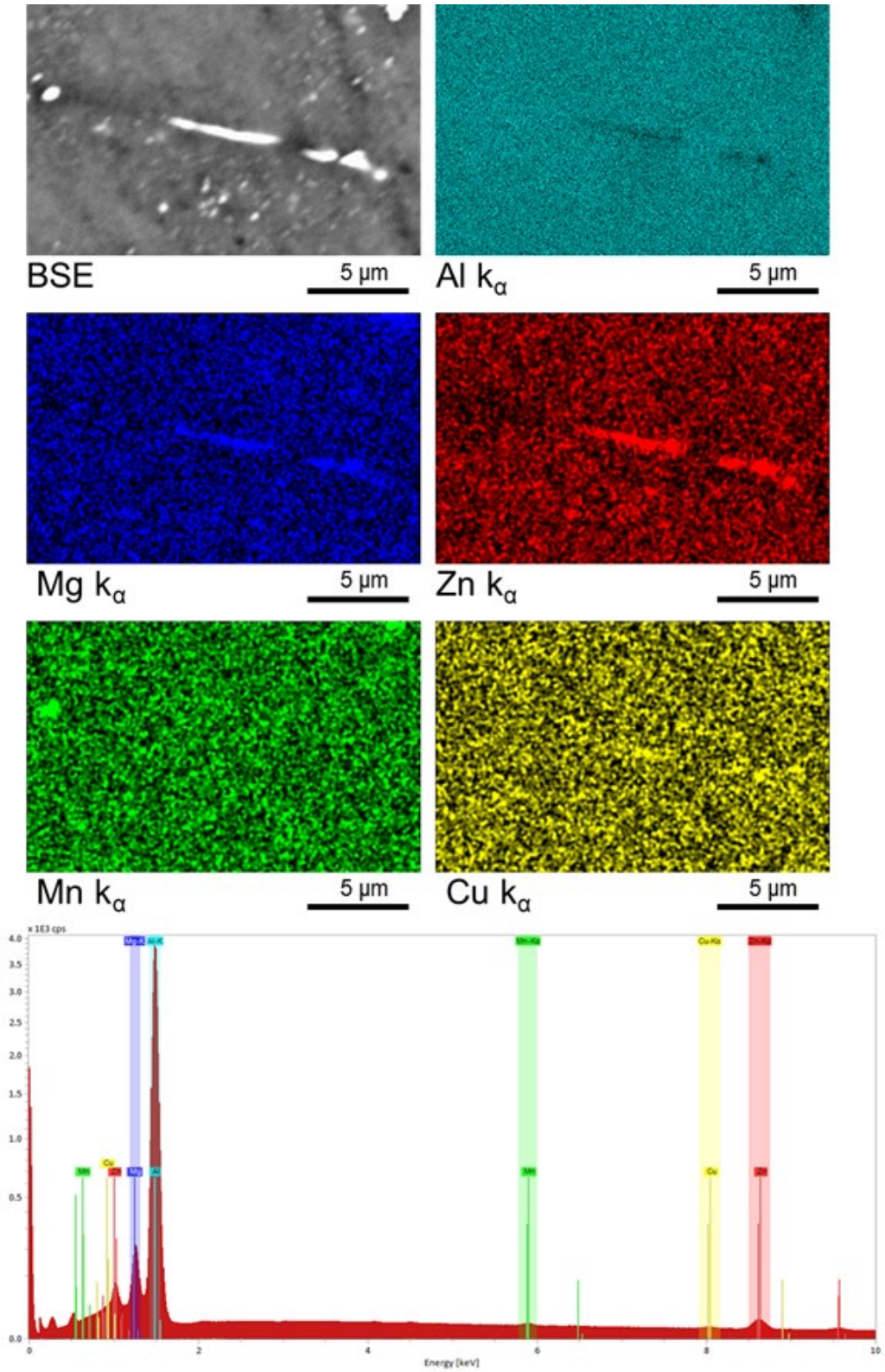

Figure 9. High-magnification EDS mapping of alloy 2B-F with EDS spectra of grain boundary precipitates. k_α energies were used to construct maps of all elements.

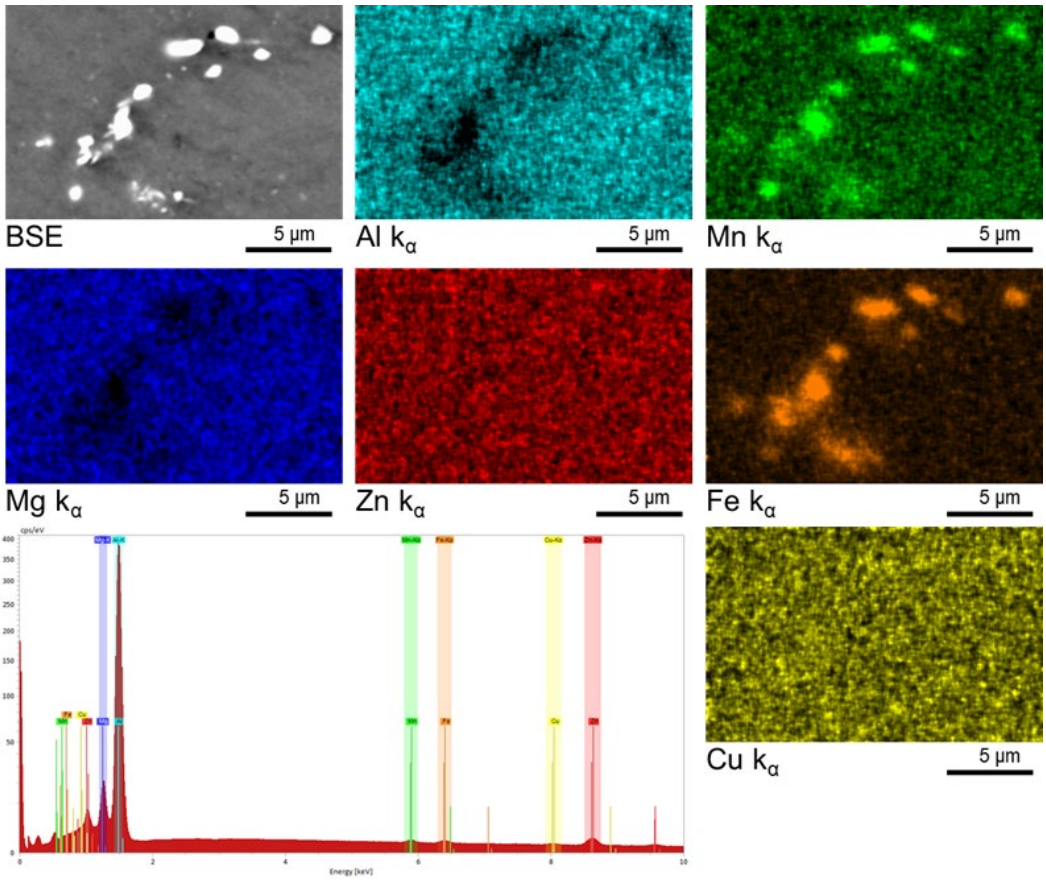

Figure 10. High-magnification EDS mapping of alloy 2B-T6 with EDS spectra of grain boundary precipitates. k_α energies were used to construct maps of all elements.

3.2 Mechanical Properties

The mechanical properties of each alloy were assessed in both the F-temper and T6-temper using HRB and tensile testing. The hardness for alloy 2A2 and 2B in both the F-temper and T6-temper were greater than the typical hardness of 5083-H131 on both the LT surface and one-half the thickness of the plate (Figure 11a). The average hardness was larger in the T6-temper than the F-temper but nearly 15 HRB lower than 5180 in a T10-temper, which is a cold-worked and peak-aged temper. An example of an engineering stress–strain curve in the TD for each alloy and temper is shown in Figure 11b with the mean values and standard deviation for the elastic modulus, yield strength, ultimate tensile strength (UTS), and percent elongation to failure for both variants of AA5180 is given in Table 3. The transverse yield strength in both tempers is below minimum qualification standard for all classes of MIL-DTL-46027M[40] plate while the UTS meets minimum specification for all classes. The only exception is alloy 2A2-T6, which did not meet the minimum value of UTS for AA5059. Both alloys in each condition showed exceptional ductility of greater than 17.2%, which far exceeds the minimum

requirements for all classes of MIL-DTL-46027M.[40] The tensile properties measured here are very promising because they were measured in the transverse direction and the tensile mechanical properties for minimum qualification on MIL-DTL-46027M[40] are for tensile bars stressed in the longitudinal direction, which typically exhibit greater strength than those measured in the transverse direction. However, the low rolling reduction here compared with a full-size industrial production ingot is expected to provide different tensile behavior, particularly in the transverse direction where grains become much more elongated in the longitudinal direction in the rolling direction.

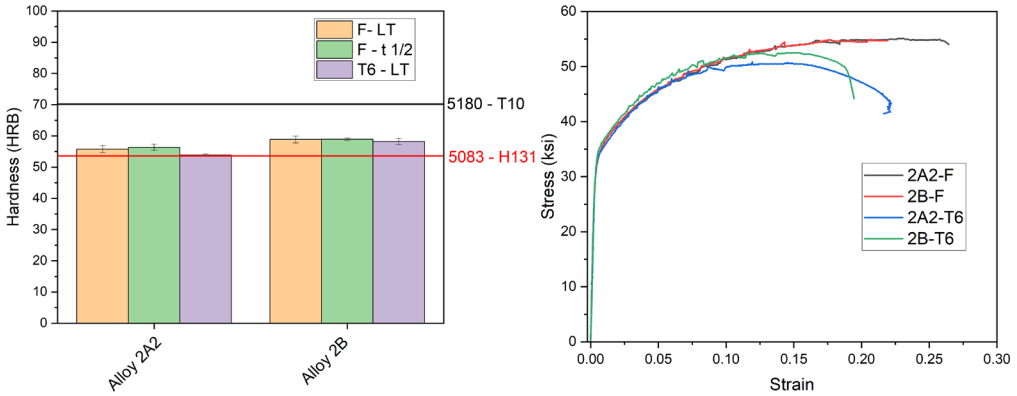

Figure 11. (a) The mean HRB measured on the LT surface and at t = 1/2 on the LS surface. (b) A typical transverse engineering stress–strain curve for each alloy in the F-temper and T6-temper. Error bars are one standard deviation of the mean.

Table 3. Mean elastic modulus (E), 0.2% yield strength ($\sigma_{0.2}$), UTS (σ_{UTS}), and % elongation to failure measured from tensile testing in transverse dog bone tensile specimens.

Alloy	E (ksi)	$\sigma_{0.2}$ (ksi)	σ_{UTS} (ksi)	%Elongation to failure
Alloy 2A2-F	10,657 ± 336	35.8 ± 0.73	53.9 ± 1.4	17.2 ± 4.9
Alloy 2A2-T6	10,231 ± 136	33.9 ± 0.70	51.0 ± 0.46	21.9 ± 0.60
Alloy 2B-F	10,0071 ± 1021	35.3 ± 0.54	54.4 ± 0.75	18.5 ± 4.3
Alloy 2B-T6	10,165 ± 1637	34.4 ± 0.38	53.1 ± 0.47	17.5 ± 4.3

Note: The ±error is one standard deviation of the mean.

3.3 C-Ring Testing

The results of C-ring testing are summarized in Table 4 where both alloys in every condition passed minimum requirements of MIL-DTL-46027M[40] and alloy 2A2-F temper passed MIL-DTL-32505B.[44] Samples in the F-temper did not fail after 28-day exposure and were removed from testing. Samples in the T6 condition passed MIL-DTL-46027M[40] for both alloys, but all samples cracked upon handling for inspection on day 15. The discrepancy of failure time between the F-temper and T6-temper requires further investigation, but residual stresses from solution

treatment and water quenching are posited to be contributing factors. In addition, anodic dissolution-induced cracking is a possibility initiated by IGC or pitting corrosion, which will be explored below, but the passing grade for both tempers is likely linked with the high tensile ductility of each alloy.

Table 4. Summary of time to failure for C-rings per the test matrix in Table 2.

Alloy	Applied load	Time to failure	Pass MIL-DTL-46027M?
Alloy 2A2-F	30 ksi	None after 28 days	All pass
Alloy 2A2-F	35 ksi	None after 28 days	All pass
Alloy 2B-F	30 ksi	None after 28 days	All pass
Alloy 2A2-T6	30 ksi	All fail on day 15	All pass
Alloy 2B-T6	30 ksi	All fail on day 15	All pass

The fracture surfaces of multiple samples were examined. An example of a typical fracture surface is given in Figure 12a for alloy 2A2-T6 and Figure 12b for alloy 2B-T6. The fracture surfaces contain smooth features typical of intergranular fracture. Some micro dimpling was observed on certain samples at high magnifications (Figure 12c), but the smooth intergranular surfaces were dominant.

Cross-sectional micrographs of cracked C-rings are shown in Figure 13 where the as-polished cross section of alloy 2A2-T6 (Figure 13a) shows the crack opening at the outer edge of the C-ring at the top of the image. The crack initiated slightly off from the centerline of the C-ring and propagated in a linear manner through the cross section with branching of the crack observed at the rear of the C-ring. The same sample of alloy 2A2-T6 was etched with Weck's reagent (Figure 13b), which confirmed that the crack path propagation followed along grain boundaries and not in a transgranular manner. The same features are observed in Figure 13c and d for a cross-sectional micrograph of alloy 2B-T6, confirming an intergranular fracture path. The as-polished sample of alloy 2A2-T6 shown in Figure 13a revealed the presence of two pits to the left of the crack initiation site, which is consistent with IGC. Thus, evidence indicates crack initiation by IGC attack.

Without knowledge of the precipitate fraction, morphology, and composition gradient and width of precipitate free zones along grain boundaries, it is difficult to provide further insight as to why the T6-temper cracked and the F-temper did not. An understanding of the grain boundary microstructure is of utmost importance because the electrochemical potential of the bulk matrix and precipitate free zone is a function of composition and the OCP can vary greatly as shown with various compositions of solution-treated crossover alloys.[35] The local dissolution and resulting chemistry at the crack tip is important for propagation of the crack with the applied stress and how the stress field of the crack tip interacts with the grain boundary microstructure. With an understanding of this, heat treatments can be

modified to tailor the grain boundary microstructure to provide increased resistance to crack initiation and propagation.

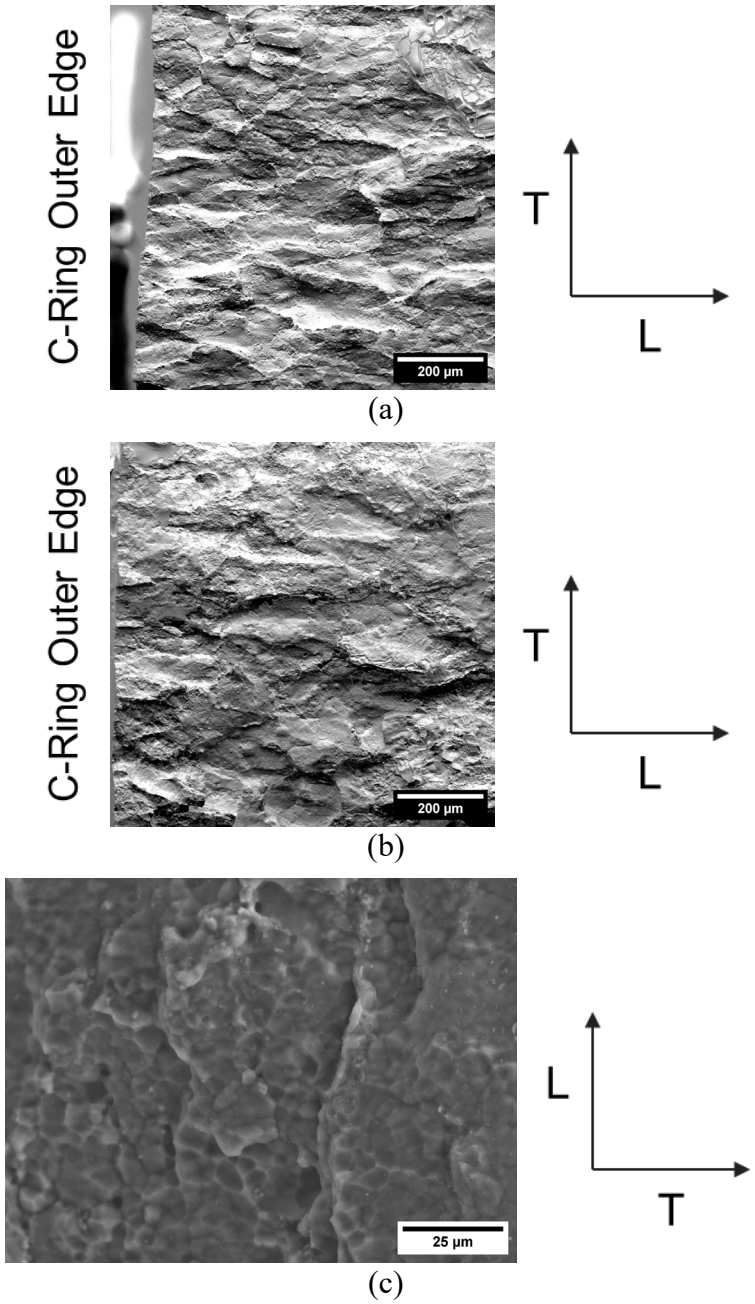

Figure 12. Fracture surfaces of (a) alloy 2A2-T6 and (b) alloy 2B-T6. (c) Higher magnification image of alloy 2A2-T6.

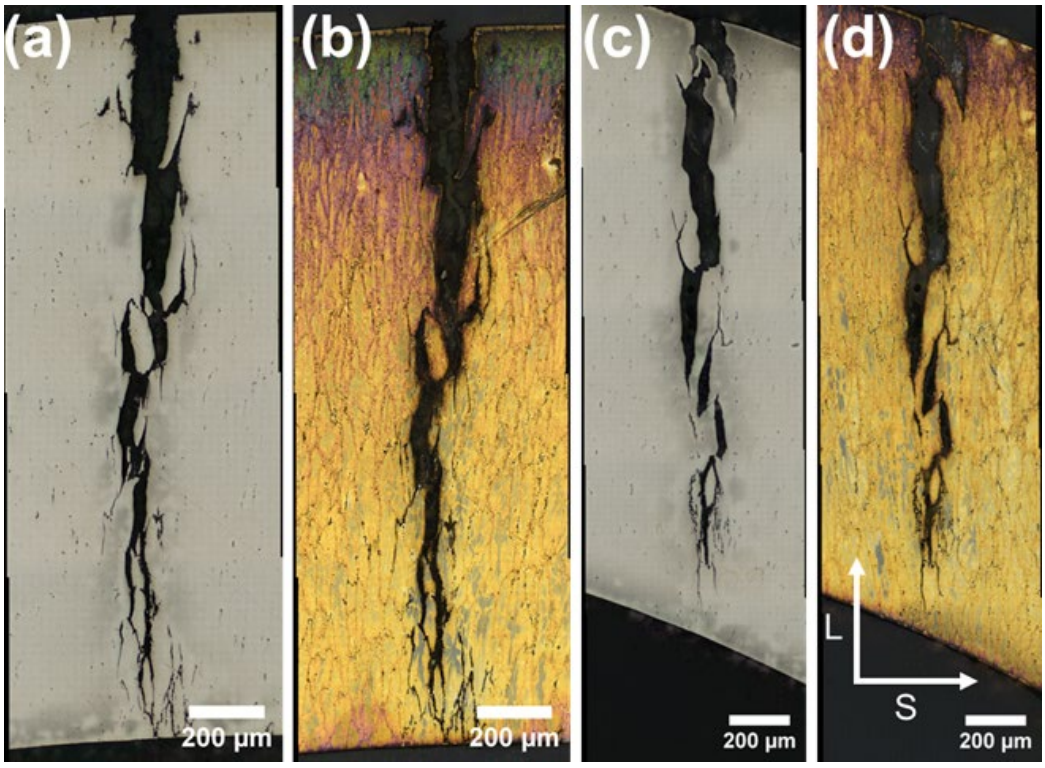

Figure 13. Cross-sectional micrographs of cracked C-rings for alloy 2A2-T6 (a) as polished and (b) etched with Weck's reagent; alloy 2B-T6 (c) as polished and (d) etched with Weck's reagent.

3.4 Electrochemical Evaluation

A median result for the OCP versus time and corresponding polarization scan is shown in Figure 14 for both alloys in each temper. The OCP versus time transient for alloy 2A2 for both tempers on the LT, SL, and ST surfaces was (Figure 14a) stabilized after the 4-h immersion time in quiescent 3.5 wt% NaCl solution. The final OCP was similar among all alloys except for alloy 2A2-T6 on the LT surface, which was more negative. The polarization scans in Figure 14b showed many notable features. The cathodic kinetics displayed a linear Tafel region from approximately −0.925 V versus sat Ag/AgCl to −1.2 V versus sat Ag/AgCl with a high slope indicating mixed mode activation control and diffusion-controlled reaction kinetics. The anodic branch displayed two linear regions: one near the corrosion potential (E_{corr}) and one at a more positive potential. The Tafel slope near E_{corr} was the steeper of the two anodic regions with the transition between the two noted as a breakdown potential (E_{bd}). The breakdown potential was not always an abrupt change in slope characteristic of pitting and was determined as the intersection point of linear fitting between the two regions. This breakdown potential is likely indicative of IGC attack given the physical observations of IGC on the C-rings in Figure 13. The mean fit values for E_{corr}, i_{corr}, β_a, β_c, E_{bd}, and the

difference between the breakdown potential and corrosion potential ($E_{bd} - E_{corr}$) measured from Tafel extrapolation is given in Table 5. For alloy 2B, the OCP was also shown to stabilize after the 4-h immersion time. The OCP of alloy 2B was slightly more noble than that of alloy 2A2, which is likely due to the additional Cu content that has been observed in other crossover alloys.[35] Meanwhile, the polarization behavior of alloy 2B possessed similar characteristic features to those described above from alloy 2A2.

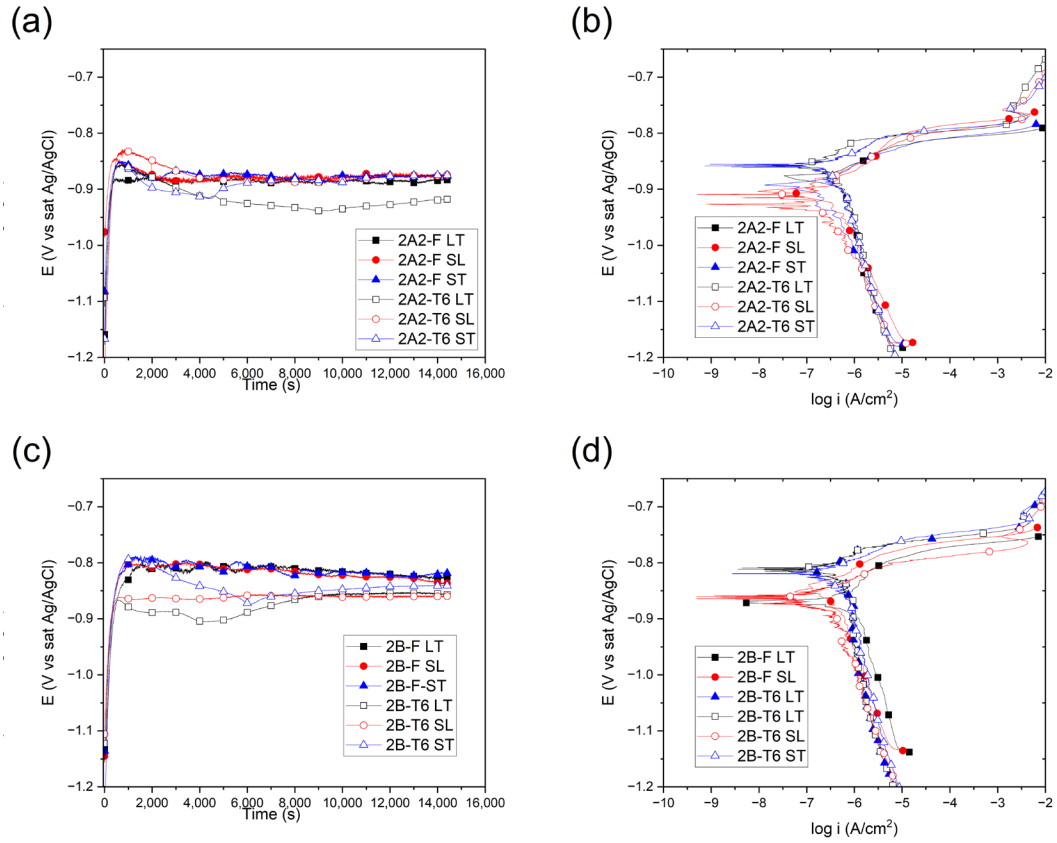

Figure 14. (a–d) Typical result from polarization scans on each alloy in the F-temper and T6-temper immersed in quiescent 3.5 wt% NaCl with a scan rate of 0.1 mV/s.

Table 5. Mean values of E_{corr}, i_{corr}, β_a, β_c, E_{bd}, and $E_{bd} - E_{corr}$ measured from Tafel extrapolation of polarization scans on each alloy in the F-temper and T6-temper.

Temper	Alloy	E_{corr} (mV vs. sat Ag/AgCl)		i_{corr} (μA/cm²)		β_a (mV/dec)		β_c (mV/dec)		E_{bd} (mV vs. sat Ag/AgCl)		$E_{bd} - E_{corr}$ (mV)	
		avg	std	avg	std	avg	std	avg	std	avg	std	avg	std
F	2A2 LT	−864	12	0.527	0.15	39.4	10	−332	96	−816	4.1	48.2	14
	2A2 SL	−886	28	0.377	0.042	59.6	22	−228	25	−808	12	78	27
	2A2 ST	−948	65	0.387	0.21	293	261	−186	64	−818	5.2	131	60
	2B LT	−863	29	2.01	1.3	66.9	22	−323	96	−809	2.4	53.2	29
	2B SL	−849	32	0.437	0.17	57.8	22	−253	26	−786	18	63	16
	2B ST	−842	11	0.503	0.22	39.4	11	−328	32	−804	2.4	38	13
T6	2A2 LT	−818	12	0.328	0.11	42.2	11	−475	137	−772	2.0	46	11
	2A2 SL	−843	67	0.301	0.12	72.8	51	−279	94	−765	25	78.2	54
	2A2 ST	−843	57	0.468	0.089	57.2	45	−347	127	−775	19	62.7	50
	2B LT	−789	14	0.581	0.09	36.7	15	−436	72	−772	4.9	22	9
	2B SL	−839	11	0.374	0.11	39.1	4.6	−290	40	−784	19	54.5	10
	2B ST	−800	13	0.677	0.20	33.7	9.5	−415	97	−761	3.1	39.0	15

NOTE: The ±error is one standard deviation (std) of the mean.

The mean E_{corr} and i_{corr} from Tafel extrapolation is provided in Figure 15 for easier visual inspection than Table 5. The E_{corr} of alloy 2A2 (Figure 15a) was measured to be relatively constant for all orientations in the T6-temper, whereas E_{corr} F-temper was measured to decrease in the order LT > SL > ST. This trend was also true for alloy 2B for the F-temper (as shown in Figure 15b), although the standard deviations for E_{corr} of alloy 2B-F were large. Meanwhile, E_{corr} of alloy 2B-T6 was more noble than that of the F-temper with E_{corr} being similar for alloy 2B-T6 LT and ST and the least noble for alloy 2B-T6 SL. The mean E_{bd}s were observed to be more noble in the T6 condition for both alloys with E_{bd} being more noble for alloy 2B versus alloy 2A2. The difference between E_{corr} and E_{bd} was the greatest on the ST surface of alloy 2A2-F due to the negative mean E_{corr}s measured. The anodic ß measured for alloy 2A2-F ST was very high at 293 mV/dec showing the presence of some diffusion-controlled anodic dissolution, but the sample-to-sample variation was also very large. All other anodic s were less than 100 mV/dec, which does not typically indicate any diffusion-controlled reactions, which is indicative of passive film formation. The origin of the high anodic Tafel slope measured on alloy 2A2-F on the ST surface is not readily apparent and requires further study.

The mean corrosion rate given in Figure 15c for alloy 2A2 and Figure 15d for alloy 2B reveals that alloy 2A2 generally has a corrosion rate lower than that of alloy 2B. For alloy 2A2, i_{corr} was lower in the T6-temper except for on the ST surface where i_{corr} was similar to that of the F-temper. In contrast, alloy 2B showed much greater variation in i_{corr} with alloy 2B-F having the highest corrosion rate on the LT surface. The corrosion rate of the F-temper decreased nearly four times from the LT surface to the SL and ST surfaces. Meanwhile, the i_{corr} of alloy 2B-T6 was highest on the

ST surface where the mean value was greater than that of the F-temper. In C-ring testing, the higher corrosion rate of the T6-temper on the ST surface could provide increased susceptibility to IGC and initiation of SCC. Furthermore, the T6-temper for both alloy compositions possessed a smaller value of $E_{bd} - E_{corr}$ on the ST surface than the F-temper, which also indicates increased susceptibility to IGC attack and could help rationalize the increased susceptibility of the T6-temper to SCC.

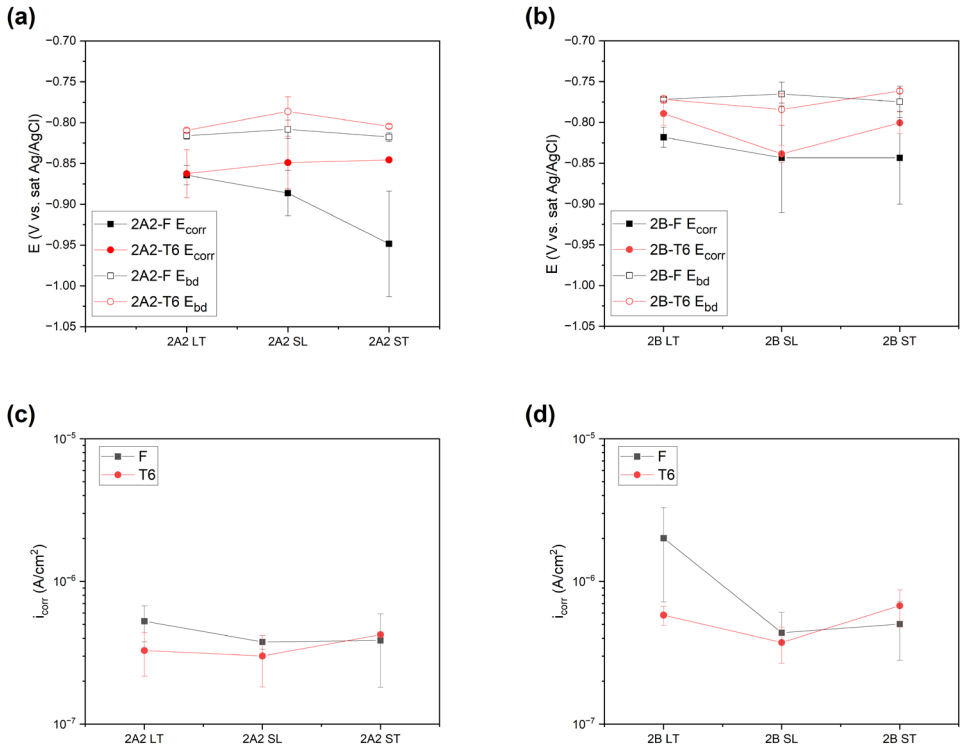

Figure 15. The mean E_{corr} (solid symbols) and E_{bd} (open symbols) for (a) alloy 2A2 and (b) alloy 2B with the mean corrosion rate for (c) alloy 2A2 and (d) alloy 2B measured from Tafel extrapolation of the polarization scans. Error bars are one standard deviation of the mean.

4. Conclusions

This study demonstrated the resistance of alloy 5180 to SCC with a low content of Cu (≈0.1 wt%) and high content of Cu (≈0.225 wt%) due to the exceptional ductility of both alloys. C-ring testing did not reveal a difference in susceptibility to SCC with Cu concentration, whereas only samples in the T6-temper cracked during the 28-day duration of the test. Cracking in the T6 condition was linked to intergranular fracture likely aided by IGC attack on the exposed alloy surface.

5. References

1. Polmear IJ. Light alloys. 4th ed. Butterworth-Heinemann; 2005.
2. Matsumoto K et al. Effects of Zn addition and aging condition on serrated flow in Al-Mg alloys. Materials Science Forum. 2014;794–796:483–488. https://doi.org/10.4028/www.scientific.net/MSF.794-796.483
3. Meng CY, Zhang D, Hua C, Zhuang LZ, Zhang JS. Mechanical properties, intergranular corrosion behavior and microstructure of Zn modified Al-Mg alloys. Journal of Alloys and Compounds. 2014;617:925–932.
4. Meng C-Y, Zhang D, Liu P-P, Zhuang L-Z, Zhang J-S. Microstructure characterization in a sensitized Al–Mg–Mn–Zn alloy. Rare Metals. 2015;37:129–135.
5. Cao C, Zhang D, He Z, Zhuang L, Zhang J. Enhanced and accelerated age hardening response of Al-5.2Mg-0.45Cu (wt%) alloy with Zn addition. Materials Science and Engineering: A. 2016;666:34–42.
6. Cao C et al. Effects of Cu addition on the precipitation hardening response and intergranular corrosion of Al-5.2Mg-2.0Zn (wt%) alloy. Materials Characterization. 2016;122:177–182.
7. Meng CY, Zhang D, Zhuang LZ, Zhang JS. Correlations between stress corrosion cracking, grain boundary precipitates and Zn content of Al-Mg-Zn alloys. Journal of Alloys and Compounds. 2016;655:178–187.
8. Cao C, Zhang D, Zhuang L, Zhang J. Improved age-hardening response and altered precipitation behavior of Al-5.2Mg-0.45Cu-2.0Zn (wt%) alloy with pre-aging treatment. Journal of Alloys and Compounds. 2017;691:40–43.
9. Hou S, Liu P, Zhang D, Zhang J, Zhuang L. Precipitation hardening behavior and microstructure evolution of Al–5.1 Mg–0.15Cu alloy with 3.0Zn (wt%) addition. Journal of Materials Science. 2017;53:3846–3861.
10. Ma QB, Zhang D, Zhuang LZ, Zhang JS. Intergranular corrosion resistance of Zn modified 5xxx series Al alloy during retrogression and re-aging treatment. Materials Characterization. 2018;144:264–273.
11. Ding QW et al. Strengthening mechanism of age-hardenable Al-Mg-3Zn alloys. Materials Science and Technology. 2019;35:1071–1080.
12. Ebenberger P, Uggowitzer PJ, Gerold B, Pogatscher S. Effect of compositional and processing variations in new 5182-type AlMgMn alloys on mechanical

properties and deformation surface quality. Materials (Basel). 2019;12(10):1645. https://www.mdpi.com/1996-1944/12/10/1645

13. Hou SL, Zhang D, Ding QW, Zhang JS, Zhuang LZ. Solute clustering and precipitation of Al-5.1Mg-0.15Cu-xZn alloy. Materials Science and Engineering: A – Structural Materials: Properties, Microstructure and Processing. 2019;759:465–478.

14. Takata N, Ishihara M, Suzuki A, Kobashi M. Microstructure and strength of a novel heat-resistant aluminum alloy strengthened by T-Al6Mg11Zn11 phase at elevated temperatures. Materials Science and Engineering: A – Structural Materials: Properties, Microstructure and Processing. 2019;739:62–70.

15. Tang HP et al. Effect of cooling rate on microstructure and mechanical properties of an Al-5.0Mg-3.0Zn-1.0Cu cast alloy. Journal of Alloys and Compounds. 2019;801:596–608.

16. Yun J, Kang S, Lee S, Bae D. Development of heat-treatable Al-5Mg alloy sheets with the addition of Zn. Materials Science and Engineering: A – Structural Materials: Properties, Microstructure and Processing. 2019;744:21–27.

17. Geng YX, Zhang D, Zhang JS, Zhuang LZ. On the suppression of Luders elongation in high-strength Cu/Zn modified 5xxx series aluminum alloy. Journal of Alloys and Compounds. 2020;834:155138.

18. Geng YX, Zhang D, Zhang JS, Zhuang LZ. Zn/Cu regulated critical strain and serrated flow behavior in Al-Mg alloys. Materials Science and Engineering: A – Structural Materials: Properties, Microstructure and Processing. 2020;795:139991.

19. Hou S et al. Dependence of microstructure, mechanical properties, and inter-granular corrosion behavior of Al-5.1Mg-3.0Zn-0.15Cu alloys with high temperature pre-treatment. Materials Characterization. 2020;168:110512.

20. Pan YL et al. Reducing welding hot cracking of high-strength novel Al-Mg-Zn-Cu alloys based on the prediction of the T-shaped device. Science and Technology of Welding and Joining. 2020;25:483–489.

21. Stemper L, Tunes MA, Oberhauser P, Uggowitzer PJ, Pogatscher S. Age-hardening response of AlMgZn alloys with Cu and Ag additions. Acta Materialia. 2020;195:541–554.

22. Tang HP et al. Effects of aging treatment on the precipitation behaviors and mechanical properties of Al-5.0Mg-3.0Zn-1.0Cu cast alloys. Journal of Alloys and Compounds. 2020;842:155707.

23. Klein T et al. Wire-arc additive manufacturing of a novel high-performance Al-Zn-Mg-Cu alloy: processing, characterization and feasibility demonstration. Additive Manufacturing. 2021;37:101663.

24. Pan YL, Zhang D, Liu HR, Zhuang LZ, Zhang JS. Precipitation hardening and intergranular corrosion behavior of novel Al-Mg-Zn(-Cu) alloys. Journal of Alloys and Compounds. 2021;853:157199.

25. Stemper L et al. Giant hardening response in AlMgZn(Cu) alloys. Acta Materialia. 2021;206:116617.

26. Takata N et al. Precipitation morphology and kinetics of T-Al6Mg11Zn11 intermetallic phase in Al-Mg-Zn ternary alloys. Intermetallics. 2021;139: 107364.

27. Zhang D et al. Friction stir welding of novel T-phase strengthened Zn-modified Al–Mg alloy. Journal of Materials Science. 2021;56:5283–5295.

28. Zhang D et al. The suppression of solidification cracking of Al welds by regulating Zn/Mg ratio. Welding in the World. 2021;65:691–698.

29. Zou Y et al. Investigation on microstructure and mechanical properties of Al-Zn-Mg-Cu alloys with various Zn/Mg ratios. Journal of Materials Science & Technology. 2021;85:106–117.

30. Liu H, Zhang Z, Zhang D, Zhang J. The effect of Ag on the tensile strength and fracture toughness of novel Al-Mg-Zn alloys. Journal of Alloys and Compounds. 2022;908:164640.

31. Stemper L, Tunes MA, Tosone R, Uggowitzer PJ, Pogatscher S. On the potential of aluminum crossover alloys. Progress in Materials Science. 2022;124:100873.

32. Zhang Z, Li Y, Li H, Zhang D, Zhang J. Effect of high Cu concentration on the mechanical property and precipitation behavior of Al–Mg–Zn-(Cu) crossover alloys. Journal of Materials Research and Technology. 2022;20:4585–4596.

33. Lei C et al. Hot deformation behavior and processing maps of an as-cast Al-5Mg-3Zn-1Cu (wt%) alloy. Materials. 2023;16:4093.

34. Zhang Z, Hao Z, Wang H, Zhang D, Zhang J. Modifying the microstructure and stress distribution of crossover Al-Mg-Zn alloy for regulating stress corrosion cracking via retrogression and re-aging treatment. Materials Science and Engineering: A. 2023;884:145564.

35. Cain TW, Blohm LM. On the corrosion behavior of precipitation hardenable 5XXX series aluminum alloys. DEVCOM Army Research Laboratory (US); 2025. Report No: ARL-TR-10126.

36. Henry Holroyd NJ, Scamans GM. Environmental degradation of marine aluminum alloys—past, present, and future. Corrosion. 2015;72:136–143.

37. Lim MLC, Kelly RG, Scully JR. Overview of intergranular corrosion mechanisms, phenomenological observations, and modeling of AA5083. Corrosion. 2015;72:198–220.

38. Crane CB, Gangloff RP. Stress corrosion cracking of Al-Mg alloy 5083 sensitized at low temperature. Corrosion. 2015;72:221–241.

39. Golumbfskie WJ et al. Survey of detection, mitigation, and repair technologies to address problems caused by sensitization of Al-Mg alloys on Navy ships. Corrosion. 2015;72:314–328.

40. MIL-DTL-46027M. Armor plate, aluminum alloy, weldable 5083, 5456, and 5059. Department of Defense (US); 2021 Sep 17.

41. ASTM B557-15. Standard test methods for tension testing wrought and cast aluminum- and magnesium-alloy products. ASTM International; 2015.

42. ASTM G38-01(2021). Standard practice for making and using C-ring stress-corrosion test specimens. ASTM International; 2021.

43. ASTM G47-20. Standard test method for determining susceptibility to stress-corrosion cracking of 2XXX and 7XXX aluminum alloy products. ASTM International; 2021.

44. MIL-DTL-32505B. Armor plate, aluminum, alloys 7017 and 7020, weldable. Department of Defense (US); 2021 Jan 21.

45. ASTM G44-21. Standard practice for exposure of metals and alloys by alternate immersion in neutral 3.5% sodium chloride solution. ASTM International; 2021.

List of Symbols, Abbreviations, and Acronyms

Al	aluminum
Ag	silver
AgCl	silver chloride
ß	Tafel slope
Bal	balance
BSE	backscattered electron
CAMI	Coated Abrasives Manufacturing Institute
Cr	chromium
Cu	copper
DI	deionized
E	elastic modulus
EAC	environmentally assisted cracking
E_{bd}	breakdown potential
E_{corr}	corrosion potential
EDS	energy dispersive X-ray spectroscopy
Fe	iron
HRB	Rockwell B hardness (scale)
i_{corr}	corrosion rate
ICP-OES	inductively coupled plasma-optical emission spectroscopy
IGC	intergranular corrosion
$KMnO_4$	potassium permanganate
LT	long-transverse
LS	long-short
Mg	magnesium
Mn	manganese
NaCl	sodium chloride

NaOH	sodium hydroxide
ND	normal direction
Ni	nickel
OCP	open circuit potential
RD	rolling direction
sat	saturated
Sc	scandium
SCC	stress corrosion cracking
SEM	scanning electron microscopy
$\sigma_{0.2}$	yield strength
Si	silicon
ST	short-transverse
Std	standard deviation
TD	transverse direction
Ti	titanium
UTS	ultimate tensile strength
wt%	weight percent
Zn	zinc
Zr	zirconium

1 (PDF)	DEFENSE TECHNICAL INFORMATION CTR DTIC OCA
1 (PDF)	DEVCOM ARL FCDD RLB CI TECH LIB